iScience

Article

Electronic transport properties in lithium cobalt oxide battery electrode material studied in ion-gated transistor configuration

Graphical abstract

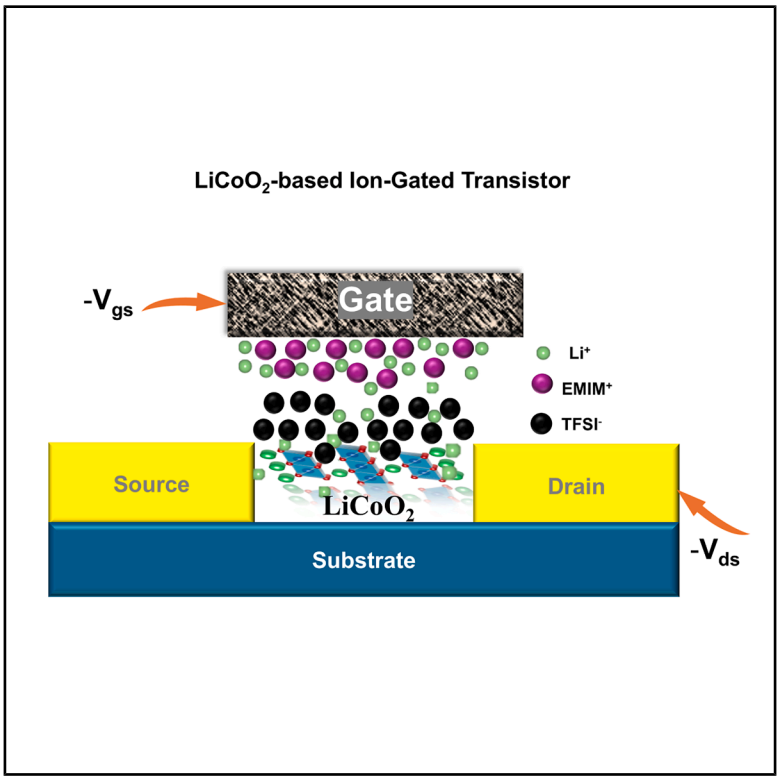

Authors

Melchiade Manirakiza, José Ramón Herrera Garza, Ramin Karimi Azari, Kesawarthini Bhaskaran, Antunes Staffolani, Francesca Soavi, Clara Santato

Correspondence

clara.santato@polymtl.ca

In brief

Chemistry; Energy engineering; Materials science

Highlights

- Ion-gated transistors enable to study *in operando* of the electronic transport of $LiCoO_2$
- In $LiCoO_2$-based channels, redox reactions take place at the surface of the channel material
- Gate-source bias controls the (de)lithiation degree in $LiCoO_2$-based channels
- The electronic conductivity of $LiCoO_2$-based channels depends on the (de)lithiation degree

Manirakiza et al., 2025, iScience *28*, 112657
June 20, 2025
https://doi.org/10.1016/j.isci.2025.112657

CellPress

iScience

CellPress
OPEN ACCESS

Article

Electronic transport properties in lithium cobalt oxide battery electrode material studied in ion-gated transistor configuration

Melchiade Manirakiza,[1,2] José Ramón Herrera Garza,[1,2] Ramin Karimi Azari,[1] Kesawarthini Bhaskaran,[1] Antunes Staffolani,[2,3] Francesca Soavi,[2,3,4] and Clara Santato[1,5,*]

[1]Department of Engineering Physics, Polytechnique Montreal, Montreal, QC H3C 3A7, Canada
[2]Department of Chemistry "Giacomo Ciamician", Alma Mater Studiorum Universitá di Bologna, Via Gobetti 85, 40129 Bologna, Italy
[3]EnerCUBE Lab, Centro di Ricerche Ambiente, Energia e Mare, Centro Interdipartimentale per la Ricerca Industriale Fonti Rinnovabili, Ambiente, Mare ed Energia (CIRI-FRAME) - Alma Mater Studiorum University of Bologna, Viale Ciro Menotti, 48, 48122 Marina di Ravenna, Italy
[4]National Reference Centre for Electrochemical Energy Storage (GISEL)-INSTM, Via G. Giusti 9, 50121 Firenze, Italy
[5]Lead contact
*Correspondence: clara.santato@polymtl.ca
https://doi.org/10.1016/j.isci.2025.112657

SUMMARY

Li-ion battery (LIB) electrode materials feature mixed electronic-ionic transport. Their electronic conductivity is expected to depend on the degree of de-lithiation/lithiation, but it is challenging to evaluate such dependence as disentangled from ionic conductivity. Herein, we use the Ion-Gated Transistor (IGT) configuration to study the dependence of the electronic conductivity of lithium cobalt oxide ($LiCoO_2$ or LCO)-based composite cathode material. LCO-based composite is employed as transistor channel interfaced with the ionic liquids: 1-Ethyl-3-methylimidazolium bis(trifluoromethylsulfonyl)imide ([EMIM][TFSI]) and 1-Butyl-1-methylpyrrolidinium bis(trifluoromethylsulfonyl)imide ($[PYR_{14}][TFSI]$), both without and with lithium bis(trifluoromethane)sulfonimide salt (LiTFSI). The gate-source bias controls the degree of lithiation/de-lithiation in the LCO composite-based IGT. We observed an increase in the drain-source transistor current upon the application of a gate-source bias, i.e., upon Li^+ de-intercalation from the LCO composite cathode material. Our results pave the way for the *in operando* evaluation of the state-of-charge (SOC) of LIB electrode materials, crucial for their efficient and sustainable use.

INTRODUCTION

Lithium-Ion Batteries (LIBs) are widely used for energy storage in different sectors, from portable electronic devices to electric vehicles and intermittent renewable energy (wind, solar) plants. They offer high energy density, high power density, and long cycle life.[1–3] LIBs use lithium-ion intercalation or insertion cathode materials that undergo reversible faradaic processes taking place in parallel with the storage/release of lithium ions (Li^+) within their crystal lattice without significant volume changes.[4,5]

During discharging of LIBs, Li^+ from the anode diffuses through the electrolyte, and it is intercalated in the cathode, while the electrons are transferred to the external circuit. This implies that the lithium-ion intercalation cathode materials are mixed ionic-electronic conductors.[6]

Electronic transport in electrode materials is one of the key factors influencing the rate performance of LIBs. Efficient electronic transport during battery operation is essential to prevent capacity loss, especially at the highest current rates.[6–8] Literature reports a dependence of the electronic conductivity of cathode materials on the rate performance and capacity fade of LIBs.[9,10] Therefore, understanding how this dependence evolves during battery operation is essential for designing high-performance LIBs.

While different cathode materials are explored, lithium cobalt oxide ($LiCoO_2$ or LCO) has been employed and is still used as an intercalation cathode material in first-generation LIBs.[11] Its charge cut-off voltage is 4.4 V vs. Li^+/Li to ensure stable output, limiting its practical capacity to 170 mAh g^{-1}, which corresponds to 60% of its theoretical capacity of 274 mAh g^{-1}.[12–14] Efforts to improve the performance of LCO cathodes include increasing the charging voltage and charging rate, ensuring the stability of both bulk and interface.[15,16]

Ménétrier et al.[17] reported a change in the electronic conductivity during Li^+ intercalation/de-intercalation in LCO, which may be associated with an insulator-to-metal transition. This transition has also been confirmed by a conductive atomic force microscopy study.[18]

Electrochemical impedance spectroscopy (EIS) has been widely used to investigate the electronic and ionic conductivity of LIB electrode materials.[19–23] The impedance is usually represented as a plot of the imaginary part versus the real part of the

impedance (Nyquist plot) acquired at different frequencies.[24] For a full or half LIB cell, the Nyquist plot describes the impedance associated with different processes that take place at the two electrodes/electrolyte interfaces and within the electrodes. At each frequency, the impedance is influenced by the process that limits the cell kinetics, specifically the slowest process at that timescale. These processes typically involve: electron transfer from the current collector to the electrode material, electronic conduction through the electrode, ionic conduction and diffusion through the electrode, and, eventually, the solid-electrolyte interface (SEI), electron transfer related to the Faradic process, and double-layer charging at the electrode/electrolyte interface.[25] Deconvoluting unambiguously the above-mentioned ionic and electronic processes by EIS is challenging: some processes could take place in the same timescale domain (similar relaxation times) and overlap in the resulting Nyquist plot.

To evaluate the electronic conductivity of LCO cathode material, ex situ studies were carried out on LCO pellets featuring different de-lithiation degrees. Four-electrode alternating current measurements run on de-intercalated LCO pellets showed an increase of six orders of magnitude for the electronic conductivity going from fully lithiated (Li_1CoO_2) to de-lithiated LCO pellets ($Li_{0.5}CoO_2$).[26] Furthermore, *ex situ* EIS experiments conducted on sintered LCO pellets placed between two ion-blocking electrodes at a temperature of 20°C permitted to deduce of a value of the electronic conductivity for LCO of ca. 6×10^{-8} S cm^{-1}.[27]

Nevertheless, *ex situ* studies do not fully reveal the dynamics of the electrochemical processes affecting the electronic conductivity of the electrode materials during battery operation. Additionally, these methods were conducted only on LCO powders, which are rarely used alone in LIBs. In real LIBs, cathode materials are usually made up of conductive additives and binders to form composites cast onto current collectors.[28] The morphology and dispersion of components significantly influence both electronic and ionic transport in composite electrodes. Introducing a small amount of conductive additive results in high electronic conductivity.[29,30]

Ion-gated transistors (IGTs) are devices where the transistor channel is in contact with an ionic gating medium (electronically insulating but ionically conductive), instead of conventional dielectrics, such as SiO_2.[31–33] The electronic conductivity of the transistor channel is modulated by the redistribution of ions upon the application of a gate-source bias.

Depending on the nature of the transistor channel and the ions in the gating medium, at least two distinct doping mechanisms, i.e., electrostatic and electrochemical, can take place. For ion-impermeable channels, ions accumulate at the interface with the channel without penetrating the channel materials, bringing about an electrostatic (two-dimensional, 2D) doping. On the other hand, with ion-permeable channels, ions enter the channel leading to an electrochemical (bulk, three-dimensional, 3D) doping.[34–37]

Recently, our groups have proposed the IGT configuration for the study of how electronic conductivity depends on the de-lithiation/lithiation degree of LIB cathode materials. We studied $LiNi_{0.5}Mn_{0.3}Co_{0.2}O_2$ (NMC532)-, $LiNi_{1.5}Mn_{0.5}O_4$ (LNMO)-based cathode materials as transistor channels.[30] Furthermore, we also used the IGT configuration to study the electronic conductivity of semiconducting materials such as LTO, TiO_2, and WO_3. Ion-gating media containing both large ions (e.g., $[EMIM]^+$, $[TFSI]^-$) and small ions (e.g., Li^+) were employed to shed light on how the nature of the ions in the ion-gating media influences the electronic transport properties of the materials, either through surface doping or intercalation into their structure.[38,39]

In this work, to assess the universality and extend the suitability of the IGT configuration to evaluate in *operando* the electronic conductivity of LIB cathode materials, we considered the case of the LCO-based composite cathode material formulated such as in real LIB cells (LCO, Super P carbon conductive additive and poly(vinylidenefluoride) (PVDF) binder with a mass ratio of 8:1:1 respectively), interfaced with the ionic liquids [EMIM][TFSI] and $[PYR_{14}][TFSI]$, in presence and absence of Li^+ (provided by the addition of LiTFSI).

Prior to the characterization of the electrochemical response and transistor characterization, we examined the structure and morphology of the LCO composite cathode material using scanning electron microscopy (SEM) and X-ray diffraction (XRD).

RESULTS AND DISCUSSION

Morphological and structural characterization of the LCO composite cathode material

We investigated the structure and morphology of the LCO composite transistor channel material deposited on a patterned SiO_2/Si substrate by XRD and SEM. The diffraction pattern featured peaks from the hexagonal phase of LCO (Joint Committee on Powder Diffraction Standards, JCPDS, 00-062-0420) (Figure S1). The value of the I_{003}/I_{104} peak intensity ratio was 2.87; literature associates values of this ratio higher than 1.2 to a low degree of cation mixing and high crystallinity for LCO.[5,40] The average crystallite size calculated using the Scherrer formula ($D = \frac{k\lambda}{\beta \cos\theta}$, with k = 0.94, λ = 1.5406 Å (Cu Kα source) and β = FWHM (full-width at half-maximum) is 47.4 nm.[41] The reflection peak 003 was used for this calculation.

SEM images (Figure S2) show that LCO samples are made up of particles with irregular geometric shapes and sizes, homogeneously distributed on the substrate, and immersed in a continuous matrix made of the carbon nanoparticles and PVDF binder.

Electrochemical response of LCO composite film in ion-gated transistor configuration

We carried out the electrochemical characterization with cyclic voltammetry (CV) in IGT configuration. The LCO composite placed between the drain and source electrodes (short-circuited) acted as the working electrode, while carbon paper coated with activated carbon acted as the reference and counter electrodes (Figure S3).[42]

Initially, we run CVs without Li salt in the ionic liquid [EMIM][TFSI], at three potential scan rates: 100 mV s^{-1}, 20 mV s^{-1} and 5 mV s^{-1}. Afterward, we run CVs in 0.1 M LiTFSI in [EMIM][TFSI]. The potential window for the CVs was −0.5 V–1.2 V vs. activated carbon (about 2.5 V–4.2 V vs. Li^+/Li).[28]

At the slowest scan rates, i.e., 5 mV s^{-1} and 20 mV s^{-1}, the cyclic voltammograms exhibit a quasi-rectangular shape without any peaks in the anodic and cathodic scans. In both measurements, with and without Li^+ in the gating medium, the current

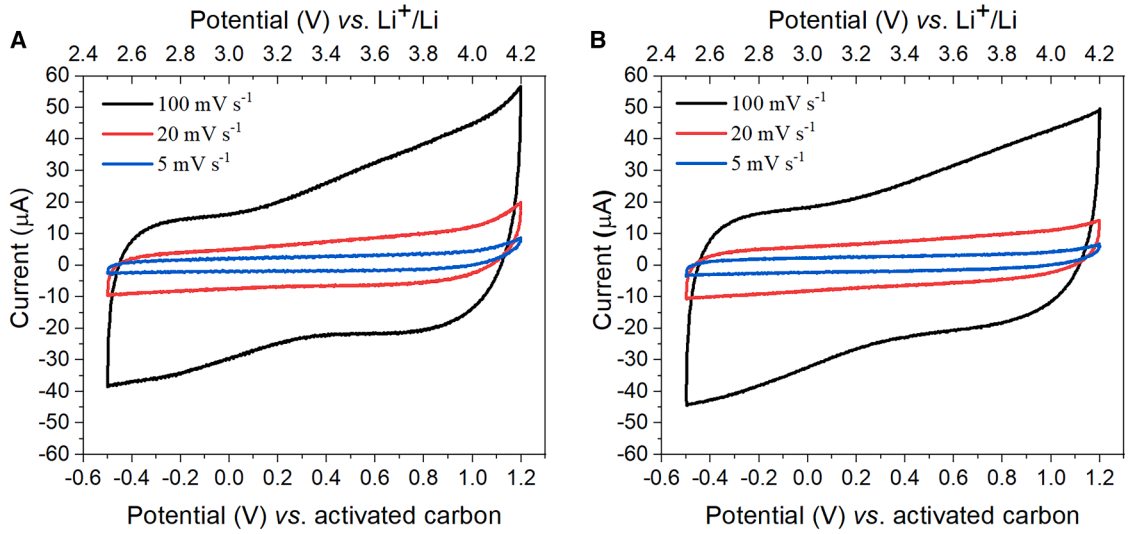

Figure 1. Cyclic voltammograms of the LCO composite at three different scan rates and ion-gating media

(A) [EMIM] [TFSI].

(B) 0.1 M LiTFSI in [EMIM][TFSI].

is proportional to the scan rate, as expected for an electrostatic charge storage mechanism, as in electrical double layer capacitors (EDLC). Only at the highest scan rate of 100 mV s^{-1}, broad anodic and cathodic peaks appear at ca. 2.8 V and 3.2 V vs. Li^+/Li, respectively (Figure 1). These peaks are typically ascribed to the Co^{4+}/Co^{3+} redox couple, but recent studies demonstrated an anionic oxygen redox mechanism without cationic contribution from cobalt during electrochemical cycling.[43]

Some materials, termed pseudocapacitive, exhibit electrochemical signatures characterized by quasi-rectangular shapes even if the charge storage mechanism includes a faradaic contribution.[44] The pseudocapacitive behavior arises when fast faradaic reactions take place on the surface or near the surface of the electrode material, and are not limited by diffusion processes.[44–46]

Hence, the cyclic voltammetry behavior of the LCO composite-based transistor channel (Figure 1) can be explained by considering the micrometric thickness of the channel (18 ± 1 μm). The thinness of the channel material causes the evolution of redox reactions typically occurring in bulk battery electrode materials toward surface reactions, accompanied by the shortening of the ion diffusion lengths, in the IGT configuration. Consequently, the LCO composite-based IGT channel material displays pseudocapacitive characteristics in the CVs.[46,47]

The unexpected poor effect of the presence of Li^+ in the [EMIM][TFSI] on the CVs brought us to further study the electrochemical response of the LCO composite in a three-electrode configuration to ensure that the current was not limited by the carbon gate in a two-electrode configuration. The results show that the currents in the three- and two-electrode configurations are of the same order of magnitude, and the shape of the CVs is similar (see Figure S4). This result indicates that in a two-electrode configuration, the current was not limited by the size of the carbon gate.

Furthermore, [EMIM][TFSI] is an ionic liquid with a pK_a value of 28.2.[48] To ascertain that the presence of acidic protons in [EMIM][TFSI] was not involved, i.e., intercalated/de-intercalated in LCO during the electrochemical process, we conducted CV measurements using the ionic liquid [PYR_{14}][TFSI] (without and with Li^+). The CV profiles exhibit similar behavior as those reported with [EMIM][TFSI], with only a slight increase in current in the presence of the lithium salt (Figure 2). Hence, even if we cannot exclude the contribution of protons, the voltametric response of the LCO composite *thin* channel material seems not much affected by the presence of Li^+ in the ion-gating medium, at least at the scan rates considered in this study.

While the prevalent mechanistic model involves the oxidation of Co^{3+} to Co^{4+} along with the Li^+ intercalation/de-intercalation, Niemöller, Jakes et al.[43] suggested a mechanism based solely on anionic oxygen oxidation. This latter mechanism does not necessitate the presence of Li^+, as it excludes the intercalation/de-intercalation mechanisms. This would suggest that, at least for *thin* channel materials, different counter-ions might not affect the CV response of the LCO composite. In addition, considering the bulky nature of the ionic liquid cations and anions, and the CV shape, we can argue that, in the actual experimental conditions, the electrochemical process mainly involves the LCO surface.

Electrical characterization of LCO composite-based ion-gated transistor

We run the transfer characteristics (drain-source current, I_{ds}, vs. gate-source voltage, V_{gs}, at fixed drain-source voltage, V_{ds}) of the LCO composite-based IGTs using [EMIM][TFSI] and [PYR_{14}][TFSI] without and with Li^+ as the gating media (Figures 3 and 4). Herein, the gate-source current, I_{gs}, results from the redistribution of the ions at the ion-gating

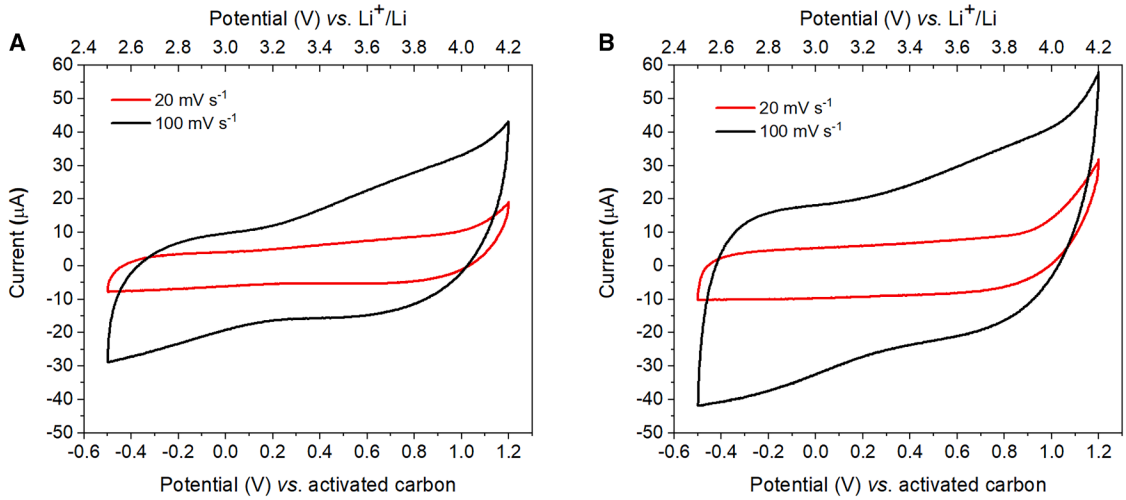

Figure 2. Cyclic voltammograms of the LCO composite at two different scan rates and ion-gating media

(A) [PYR_{14}][TFSI].

(B) 1 M LiTFSI in [PYR_{14}][TFSI].

medium/carbon gate interface, while I_{ds} corresponds to the current flowing through the LCO composite channel included between the source and drain electrodes.

In [EMIM][TFSI], I_{ds} decreases slightly from V_{gs} = 0.5 V–0.2 V and then increases from V_{gs} = 0.2 V to −1.2 V (Figures 3A–3C). In the presence of Li^+ (Figures 3D–3F), I_{ds} decreases for V_{gs} values higher than 0.3 V and then increases from V_{gs} = 0.3 V to −1.2 V. The transistor onset voltages are ca. 0.2 V in [EMIM][TFSI] and ca. 0.3 V in the presence of Li^+ in the ion-gating medium, at all scan rates. The ON/OFF ratio values were 1.01 for [EMIM][TFSI] and 1.02 for 0.1 M LiTFSI in [EMIM][TFSI] at all V_{gs} scan rates (Table S1).

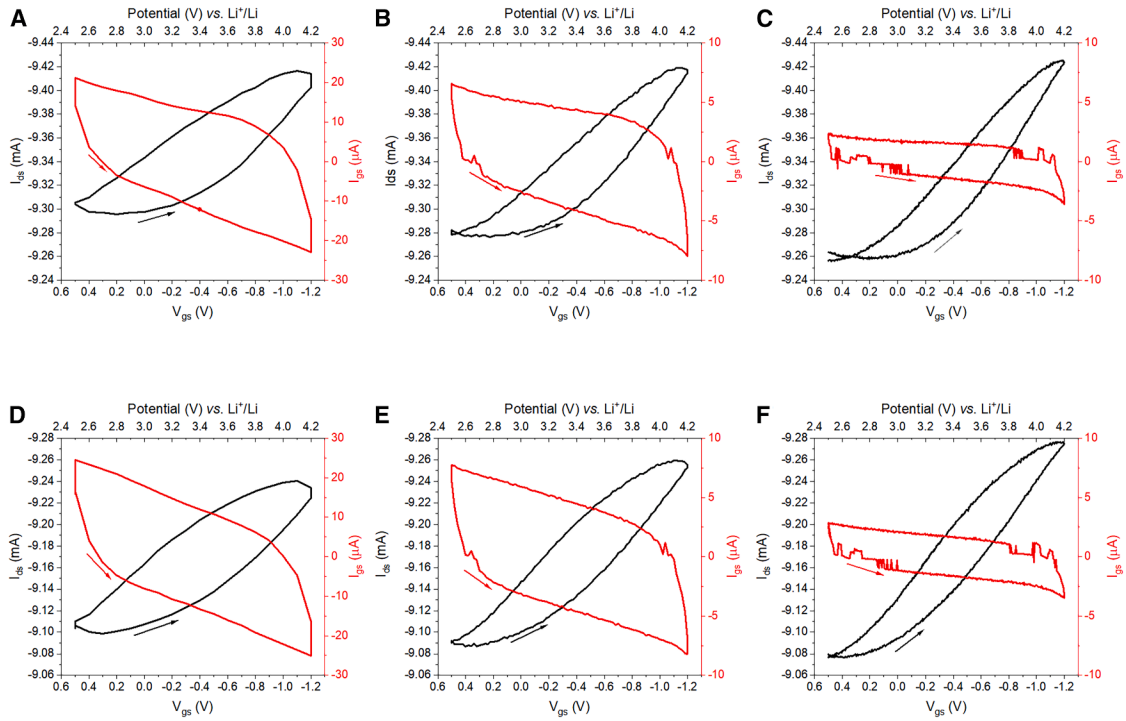

Figure 3. Transfer curves (I_{ds} vs. $V_{gs}, V_{ds} = -200\ mV$) of LCO composite at different V_{gs} scan rates of: 100 mV s^{-1} (A and D), 20 mV s^{-1} (B and E), and 5 mV s^{-1} (C and F)

Ion-gating media: [EMIM][TFSI] (A, B, and C) and 0.1 M LiTFSI in [EMIM][TFSI] (D, E, and F).

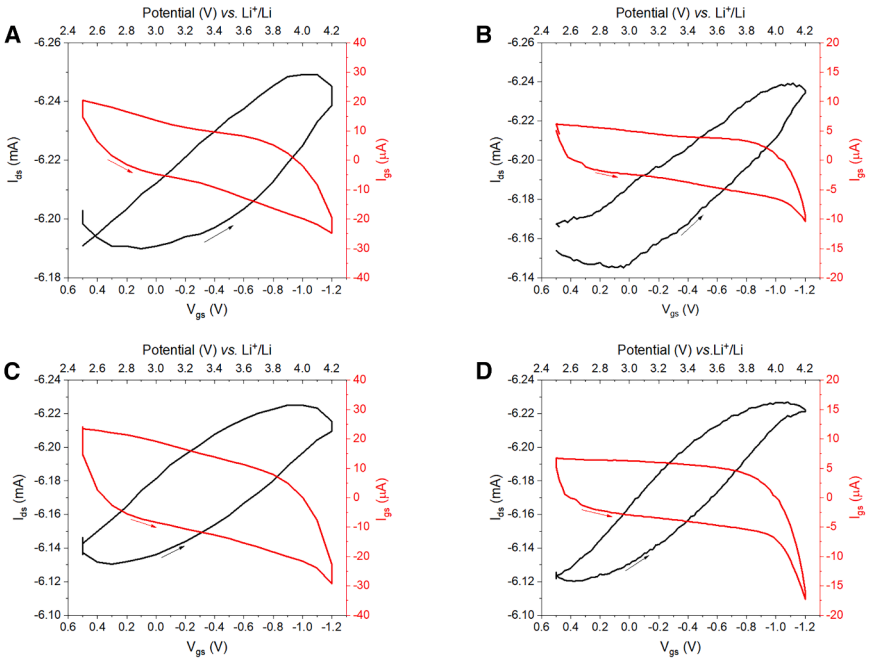

Figure 4. Transfer curves (I_{ds} vs. V_{gs}, $V_{ds} = -200\,mV$) of LCO composite at different V_{gs} scan rates of: 100 mV s^{-1} (A and C) and 20 mV s^{-1} (B and D)

Ion-gating media: [PYR_{14}][TFSI] (A and B) and 1 M LiTFSI in [PYR_{14}][TFSI] (C and D).

In [PYR_{14}][TFSI] ionic liquid, the decrease in I_{ds} is observed for V_{gs} higher than 0 V and then increases for V_{gs} values below 0 V (Figures 4A and 4B), while in 1M LiTFSI [PYR_{14}][TFSI], I_{ds} decreases for V_{gs} above 0.3 V and increases from V_{gs} = 0.3 V to −1.2 V (Figures 4C and 4D).

From the transfer curves, we calculated the charge carrier density n by the Equation 1[32]:

$$n = \frac{Q}{e\,A} = \frac{\left(\int I_{gs}\,dV_{gs}\right)}{r_v\,e\,A} \qquad \text{(Equation 1)}$$

Where Q is the charge accumulated in the channel during the forward scan, e is the elementary charge (1.6×10^{-19} C), A is the geometric area of the film exposed to the ion-gating medium (4×10^{-2} cm^2), and r_v is the V_{gs} scan rate.

The charge carrier mobility, μ, was obtained by the Equation 2:

$$\mu = \frac{L\,I_{ds}}{n\,e\,W\,V_{ds}} \qquad \text{(Equation 2)}$$

Where L is the drain-source interelectrode distance (10 μm) and W is the width of the channel (4 mm).

Tables 1 and 2 report the values of accumulated charge Q, charge carrier density n and mobility μ, different ion-gating media, at different scan rates.

The increase in I_{ds} with V_{gs} (in both gating media) is related to the oxidation of the cobalt paralleled by the extraction of Li^+ from the LCO film (delithiation process). Such an increase indicates the change in electronic conductivity in the LCO composite-based transistor channel as previously reported in an ex situ study of LCO pellets.[26,27] As observed in CVs curves, there is no significant difference in the increase of I_{ds} values in [EMIM][TFSI] or [PYR_{14}][TFSI] without or with Li^+, in the transfer characterics.

The high values of I_{ds} observed for low (absolute) values of V_{gs} in the transfer curves are due to the presence of the conductive carbon additive in the LCO composite. This results in high I_{OFF} (the current measured in the OFF state, where V_{gs} = 0) values, in turn bringing to low ON/OFF ratios (Table S1).

The highest charge carrier densities n were obtained for the V_{gs} scan rate of 5 mV s^{-1} (5.7×10^{16} cm^{-2} in [EMIM][TFSI] and 6×10^{16} cm^{-2} in [EMIM][TFSI] with Li^+) and 20 mV s^{-1} (3.6×10^{16} cm^{-2} in [PYR_{14}][TFSI]) and 4.5×10^{16} cm^{-2} for [PYR_{14}][TFSI] with Li). This indicates that the slower V_{gs} scan rate facilitates the oxidation/reduction of the LCO composite, resulting in higher charge carrier density, n, which in turn implies greater electronic conductivity in the LCO composite transistor channel.

However, the presence of binder and conductive carbon additive in the LCO composite affects the charge carrier densities.[29] Therefore, these values of charge carrier densities cannot be attributed to the LCO alone but rather to the composite made up of LCO, binder and conductive additive.

Furthermore, we studied the output transistor characteristics of LCO composite-based IGTs (e.g., [EMIM][TFSI] without and with Li^+) for V_{gs} ranging from 0 V to −1.2 V, corresponding to the potential from 3 V to 4.2 V vs. Li^+/Li, with V_{gs} = −0.6 V steps, at a V_{ds} scan rate of 20 mV s^{-1}. The I_{ds} vs. V_{ds} plots (Figures S5 and S6) show the ohmic nature of the LCO-based composite material. The resistance can be estimated from the slope of the I_{ds} vs. V_{ds} plots. For increasingly negative values of V_{gs}, the resistance decreases due to the delithiation of the LCO composite material (Table S2; S3). This finding agrees with other works reported in the literature, but has been obtained by ex situ or DC polarization techniques.[26,27]

Conclusions

In conclusion, we demonstrated the use of the IGT configuration to monitor the change in electronic current of LCO-based composite cathode material using the ionic liquids [EMIM][TFSI] and [PYR_{14}][TFSI], both with and without Li^+ as the gating media. The IGTs characterized in this study operate in depletion mode upon the application of a gate bias that induces the de-lithiation/lithiation processes in the LCO composite transistor channel.

We observed an increase in the drain-source (electronic) current for negative V_{gs} values, as related to the lithiation/de-lithiation

Table 1. Values of accumulated charge (Q), charge carrier density (n) and mobility (μ) in [EMIM][TFSI] without and with Li^+, at scan rates of 100, 20 and 5 mV s^{-1}

	[EMIM][TFSI]			0.1 M LiTFSI in [EMIM][TFSI]		
Scan rate	100 mV s^{-1}	20 mV s^{-1}	5 mV s^{-1}	100 mV s^{-1}	20 mV s^{-1}	5 mV s^{-1}
Q (C)	(1.6 ± 0.2) x 10^{-4}	(2.8 ± 0.4) x 10^{-4}	(3.6 ± 0.8) x 10^{-4}	(1.8 ± 0.2) x 10^{-4}	(3.1 ± 0.4) x 10^{-4}	(4.3 ± 0.7) x 10^{-4}
μ (cm^2 V^{-1} s^{-1})	(2.8 ± 0.4) x 10^{-2}	(1.6 ± 0.2) x 10^{-2}	(1.3 ± 0.3) x 10^{-2}	(2.5 ± 0.2) x 10^{-2}	(1.4 ± 0.1) x 10^{-2}	(1.1 ± 0.2) x 10^{-2}
n (cm^{-2})	(2.6 ± 0.4) x 10^{16}	(4.5 ± 0.6) x 10^{16}	(5.7 ± 1.3) x 10^{16}	(2.8 ± 0.4) x 10^{16}	(4.9 ± 0.6) x 10^{16}	(6.6 ± 1.1) x 10^{16}

processes. The pseudocapacitive characteristics observed by cyclic voltammetry in our thin LCO composite channels suggest surface-dominated redox processes, that potentially involve anionic oxygen, thereby minimizing reliance on Li^+ intercalation. The negligible impact of the presence of Li^+ in the ionic liquid gating media further supports this mechanistic hypothesis, at least in the IGT configuration. Charge carrier density depends on scan rate, with slower scan rates enabling higher charge accumulation, consistent with ion redistribution dynamics. Furthermore, our results highlight the potential of IGT configuration as a tool for evaluating *in operando* the electronic current as disentangled from the ionic current in LIB electrode materials.

In perspective, future studies in collaboration with Argonne National Laboratory will utilize advanced *in operando* techniques, such as X-ray absorption spectroscopy, X-ray diffraction, and neutron imaging, to capture real-time structural and electronic changes during cycling. This approach will elucidate the interplay between SOC-dependent structural transitions and electronic transport in LIBs, for the development of more durable and high-performance LIBs.

Limitation of the study

Our study was not able to follow the chemical changes during IGT operation. Conducting a chemical characterization study *in operando* in IGT configuration (e.g., XPS *in operando*) could provide valuable information on the chemical changes occurring in the material during IGT operation, thus leading to a better understanding of the *doping/de-doping* mechanism.

RESOURCE AVAILABILITY

Lead contact

Further information and requests for resources and reagents should be directed to and will be fulfilled by the lead contact, Clara Santato (clara.santato@polymtl.ca).

Materials availability

This study did not generate new unique materials.

Data and code availability

- The dataset used in this article will be shared by the lead contact upon reasonable request.
- No original code was generated in this study.
- Any information related to this study is available from the lead contact upon request.

ACKNOWLEDGMENTS

The authors are grateful to Yves Drolet for his technical support. C.S. acknowledges NSERC (Discovery Grant) and the Canada Research Chairs. C. S. and F. S. to Institut de l'énergie Trottier, for financial support. F. S. and A. S. acknowledge MOST - Sustainable Mobility Center project, funded by the European Union Next-Generation EU (PIANO NAZIONALE DI RIPRESA E RESILIENZA (PNRR) and MISSIONE 4 COMPONENTE 2, INVESTIMENTO 1.4 e D.D. 1033 17/06/2022, CN00000023.

AUTHOR CONTRIBUTIONS

Conceptualization, C.S. and F.S.; methodology, M.M., C.S., and F.S.; investigation, M.M., writing– original draft, M.M.; writing – review and editing, J.R.H., A.S., R.K.A., K.B., C.S., and F.S.; funding acquisition, C.S. and F.S.; resources, C.S.; supervision, C.S. and F.S.

DECLARATION OF INTERESTS

The authors declare no competing interests.

STAR★METHODS

Detailed methods are provided in the online version of this paper and include the following:

- KEY RESOURCES TABLE
- METHOD DETAILS
  - LCO composite ink
  - Ion-gating media
  - Electrodes fabrications
  - LCO films deposition
  - Device assembly
  - Electrochemical response and IGT characterization
  - Material characterizations

Table 2. Values of accumulated charge (Q), charge carrier density (n) and mobility (μ) in [PYR_{14}] [TFSI] without and with Li^+, at scan rates of 100 and 20 mV s^{-1}

	[PYR_{14}][TFSI]		1 M LiTFSI in [PYR_{14}][TFSI]	
Scan rate	100 mV s^{-1}	20 mV s^{-1}	100 mV s^{-1}	20 mV s^{-1}
Q (C)	(1.2 ± 0.5) x 10^{-4}	(2.3 ± 1.2) ×10^{-4}	(1.5 ± 0.7) x 10^{-4}	(2.9 ± 1.1) ×10^{-4}
μ (cm^2 V^{-1} s^{-1})	(2.9 ± 1.3) x 10^{-2}	(1.6 ± 0.8) x 10^{-2}	(2.3 ± 1.2) x 10^{-2}	(1.2 ± 0.4) x 10^{-2}
n (cm^{-2})	(1.8 ± 0.8)x 10^{16}	(3.6 ± 1.8) x 10^{16}	(2.6 ± 1.1) x 10^{16}	(4.5 ± 1.7) x 10^{16}

SUPPLEMENTAL INFORMATION

Supplemental information can be found online at https://doi.org/10.1016/j.isci.2025.112657.

Received: March 7, 2025
Revised: April 16, 2025
Accepted: May 9, 2025
Published: May 13, 2025

REFERENCES

1. Kim, T., Song, W., Son, D.-Y., Ono, L.K., and Qi, Y. (2019). Lithium-ion batteries: outlook on present, future, and hybridized technologies. J. Mater. Chem. A Mater. *7*, 2942–2964. https://doi.org/10.1039/C8TA10513H.
2. Mohamed, N., and Allam, N.K. (2020). Recent advances in the design of cathode materials for Li-ion batteries. RSC Adv. *10*, 21662–21685. https://doi.org/10.1039/D0RA03314F.
3. Kaushik, S., Mehta, T., Chand, P., Sharma, S., and Kumar, G. (2024). Recent advancements in cathode materials for high-performance Li-ion batteries: Progress and prospects. J. Energy Storage *97*, 112818. https://doi.org/10.1016/j.est.2024.112818.
4. Chen, S., Zhao, D., Chen, L., Liu, G., Ding, Y., Cao, Y., and Chen, Z. (2021). Emerging Intercalation Cathode Materials for Multivalent Metal-Ion Batteries: Status and Challenges. Small Struct. *2*, 2100082. https://doi.org/10.1002/sstr.202100082.
5. Shen, X., Zhang, X.-Q., Ding, F., Huang, J.-Q., Xu, R., Chen, X., Yan, C., Su, F.-Y., Chen, C.-M., Liu, X., and Zhang, Q. (2021). Advanced Electrode Materials in Lithium Batteries: Retrospect and Prospect. Energy Mater. Adv. *2021*. https://doi.org/10.34133/2021/1205324.
6. Byles, B.W., Palapati, N.K.R., Subramanian, A., and Pomerantseva, E. (2016). The role of electronic and ionic conductivities in the rate performance of tunnel structured manganese oxides in Li-ion batteries. APL Mater. *4*. https://doi.org/10.1063/1.4948272.
7. Tian, R., Park, S.-H., King, P.J., Cunningham, G., Coelho, J., Nicolosi, V., and Coleman, J.N. (2019). Quantifying the factors limiting rate performance in battery electrodes. Nat. Commun. *10*, 1933. https://doi.org/10.1038/s41467-019-09792-9.
8. Akhtar, S., Lee, W., Kim, M., Park, M.-S., and Yoon, W.-S. (2021). Conduction Mechanism of Charge Carriers in Electrodes and Design Factors for the Improvement of Charge Conduction in Li-ion Batteries. J. Electrochem. Sci. Technol. *12*, 1–20. https://doi.org/10.33961/jecst.2020.01564.
9. Jang, J., Im, H., Koo, J.K., Kim, M.S., Mun, J., and Kim, Y.-J. (2025). Exploring the distinct effects of ionic and electronic conductivities of cathodes on the electrochemical performance of lithium-ion batteries. J. Energy Storage *114*, 115935. https://doi.org/10.1016/j.est.2025.115935.
10. Pouraghajan, F., Thompson, A.I., Hunter, E.E., Mazzeo, B., Christensen, J., Subbaraman, R., Wray, M., and Wheeler, D. (2021). The effects of cycling on ionic and electronic conductivities of Li –ion battery electrodes. J. Power Sources *492*, 229636. https://doi.org/10.1016/j.jpowsour.2021.229636.
11. Zhang, J.C., Liu, Z.D., Zeng, C.H., Luo, J.W., Deng, Y.D., Cui, X.Y., and Chen, Y.N. (2022). High-voltage LiCoO2 cathodes for high-energy-density lithium-ion battery. Rare Met. *41*, 3946–3956. https://doi.org/10.1007/s12598-022-02070-6.
12. Bi, Z., Zhang, A., Wang, G., Dong, C., Das, P., Shi, X., and Wu, Z.-S. (2024). Hybrid ion/electron interfacial regulation stabilizes the cobalt/oxygen redox of ultrahigh-voltage lithium cobalt oxide for fast-charging cyclability. Sci. Bull. *69*, 2071–2079. https://doi.org/10.1016/j.scib.2024.04.015.
13. Gao, H., Meng, Y., Liu, X., and Zhu, F. (2022). Improvement of electrochemical properties of LiCoO2 at 4.6 V by a LiPAA coating. J. Mater. Sci. Mater. Electron. *33*, 17125–17136. https://doi.org/10.1007/s10854-022-08588-w.
14. Chen, Z., and Dahn, J.R. (2004). Methods to obtain excellent capacity retention in LiCoO2 cycled to 4.5 V. Electrochim. Acta *49*, 1079–1090. https://doi.org/10.1016/j.electacta.2003.10.019.
15. Song, S., Li, Y., Yang, K., Chen, Z., Liu, J., Qi, R., Li, Z., Zuo, C., Zhao, W., Yang, N., et al. (2021). Interplay between multiple doping elements in high-voltage $LiCoO_2$. J. Mater. Chem. A Mater. *9*, 5702–5710. https://doi.org/10.1039/D0TA09931G.
16. Wang, G., Bi, Z., Zhang, A., Das, P., Lin, H., and Wu, Z.-S. (2024). High-Voltage and Fast-Charging Lithium Cobalt Oxide Cathodes: From Key Challenges and Strategies to Future Perspectives. Engineering *37*, 105–127. https://doi.org/10.1016/j.eng.2023.08.021.
17. Ménétrier, M., Saadoune, I., Levasseur, S., and Delmas, C. (1999). The insulator-metal transition upon lithium deintercalation from LiCoO2: electronic properties and 7Li NMR study. J. Mater. Chem. *9*, 1135–1140. https://doi.org/10.1039/A900016J.
18. Kang, H., Lee, J., Rodgers, T., Shim, J.-H., and Lee, S. (2019). Electrical Conductivity of Delithiated Lithium Cobalt Oxides: Conductive Atomic Force Microscopy and Density Functional Theory Study. J. Phys. Chem. C *123*, 17703–17710. https://doi.org/10.1021/acs.jpcc.9b03232.
19. Wang, L., Zhao, J., He, X., Gao, J., Li, J., Wan, C., and Jiang, C. (2012). Electrochemical Impedance Spectroscopy (EIS) Study of LiNi1/3Co1/3Mn1/3O2 for Li-ion Batteries. Int. J. Electrochem. Sci. *7*, 345–353. https://doi.org/10.1016/S1452-3981(23)13343-8.
20. Zhuang, Q.-C., Wei, T., Du, L.-L., Cui, Y.-L., Fang, L., and Sun, S.-G. (2010). An Electrochemical Impedance Spectroscopic Study of the Electronic and Ionic Transport Properties of Spinel LiMn2O4. J. Phys. Chem. C *114*, 8614–8621. https://doi.org/10.1021/jp9109157.
21. Nobili, F., Tossici, R., Marassi, R., Croce, F., and Scrosati, B. (2002). An AC Impedance Spectroscopic Study of LixCoO2 at Different Temperatures. J. Phys. Chem. B *106*, 3909–3915. https://doi.org/10.1021/jp013569a.
22. Reddy, M.V., Subba Rao, G.V., and Chowdari, B.V.R. (2007). Preparation and Characterization of LiNi0.5Co0.5O2 and LiNi0.5Co0.4Al0.1O2 by Molten Salt Synthesis for Li Ion Batteries. J. Phys. Chem. C *111*, 11712–11720. https://doi.org/10.1021/jp0676890.
23. Qiu, X.-Y., Zhuang, Q.-C., Zhang, Q.-Q., Cao, R., Ying, P.-Z., Qiang, Y.-H., and Sun, S.-G. (2012). Electrochemical and electronic properties of LiCoO2 cathode investigated by galvanostatic cycling and EIS. Phys. Chem. Chem. Phys. *14*, 2617–2630. https://doi.org/10.1039/C2CP23626E.
24. Meddings, N., Heinrich, M., Overney, F., Lee, J.-S., Ruiz, V., Napolitano, E., Seitz, S., Hinds, G., Raccichini, R., Gaberšček, M., and Park, J. (2020). Application of electrochemical impedance spectroscopy to commercial Li-ion cells: A review. J. Power Sources *480*, 228742. https://doi.org/10.1016/j.jpowsour.2020.228742.
25. Gaberšček, M. (2021). Understanding Li-based battery materials via electrochemical impedance spectroscopy. Nat. Commun. *12*, 6513. https://doi.org/10.1038/s41467-021-26894-5.
26. Milewska, A., Swierczek, K., Tobola, J., Boudoire, F., Hu, Y., Bora, D.K., Mun, B.S., Braun, A., and Molenda, J. (2014). The Nature of the Nonmetal-Metal Transition in LiCoO2 Oxide. Solid State Ionics *263*, 110–118. https://doi.org/10.1016/j.ssi.2014.05.011.
27. Wang, S., Yan, M., Li, Y., Vinado, C., and Yang, J. (2018). Separating electronic and ionic conductivity in mix-conducting layered lithium transition-metal oxides. J. Power Sources *393*, 75–82. https://doi.org/10.1016/j.jpowsour.2018.05.005.
28. Costa, C.M., Gonçalves, R., and Lanceros-Méndez, S. (2019). Advances in Cathode Nanomaterials for Lithium-Ion Batteries. In Nanostructured Materials for Next-Generation Energy Storage and Conversion: Advanced Battery and Supercapacitors, Q. Zhen, S. Bashir, and J.L. Liu, eds. (Springer Berlin Heidelberg), pp. 105–145. https://doi.org/10.1007/978-3-662-58675-4_3.

29. Kondo, H., Sawada, H., Okuda, C., and Sasaki, T. (2019). Influence of the Active Material on the Electronic Conductivity of the Positive Electrode in Lithium-Ion Batteries. J. Electrochem. Soc. *166*, A1285–A1290. https://doi.org/10.1149/2.0051906jes.

30. Poli, F., Herrera, J.R., Lan, T., Kumar, P., Santato, C., and Soavi, F. (2023). Electronic properties of lithium-ion battery cathodes studied in ion-gated transistor configuration. iScience *26*, 105888. https://doi.org/10.1016/j.isci.2022.105888.

31. Karimi Azari, R., Lan, T., and Santato, C. (2023). On the factors affecting the response time of synaptic ion-gated transistors. J. Mater. Chem. C Mater. *11*, 8293–8299. https://doi.org/10.1039/D3TC00161J.

32. S Barbosa, M., M B Oliveira, F., Meng, X., Soavi, F., Santato, C., and O Orlandi, M. (2018). Tungsten oxide ion gel-gated transistors: how structural and electrochemical properties affect the doping mechanism. J. Mater. Chem. C Mater. *6*, 1980–1987. https://doi.org/10.1039/C7TC04529H.

33. Meng, X., Quenneville, F., Venne, F., Di Mauro, E., Işık, D., Barbosa, M., Drolet, Y., Natile, M.M., Rochefort, D., Soavi, F., and Santato, C. (2015). Electrolyte-Gated WO3 Transistors: Electrochemistry, Structure, and Device Performance. J. Phys. Chem. C *119*, 21732–21738. https://doi.org/10.1021/acs.jpcc.5b09089.

34. Liu, G., Guo, Y., and Liu, Y. (2024). Design of ion-gated transistor materials at the molecular level. Matter *7*, 430–455. https://doi.org/10.1016/j.matt.2023.11.024.

35. Bu, X., Xu, H., Shang, D., Li, Y., Lv, H., and Liu, Q. (2020). Ion-Gated Transistor: An Enabler for Sensing and Computing Integration. Advanced Intelligent Systems *2*, 2000156. https://doi.org/10.1002/aisy.202000156.

36. Sun, C., Liu, X., Jiang, Q., Ye, X., Zhu, X., and Li, R.-W. (2023). Emerging electrolyte-gated transistors for neuromorphic perception. Sci. Technol. Adv. Mater. *24*, 2162325. https://doi.org/10.1080/14686996.2022.2162325.

37. Xiang, L., Liu, L., Zhang, F., Di, C.-a., and Zhu, D. (2021). Ion-Gating Engineering of Organic Semiconductors toward Multifunctional Devices. Adv. Funct. Mater. *31*, 2102149. https://doi.org/10.1002/adfm.202102149.

38. Karimi Azari, R., Camargo, L.P., Garza, J.R.H., Collins, L., Yu Tsai, W., Neres, L.C.d.S., Dang, P., Barbosa, M.S., and Santato, C. (2025). Emulation of Synaptic Plasticity in WO3-Based Ion-Gated Transistors. Advanced Electronic Materials, 2400807. https://doi.org/10.1002/aelm.202400807.

39. Garza, J.R.H., Camargo, L.P., Azari, R.K., Neres, L.C.d.S., Khaleel, S., Barbosa, M.S., Soavi, F., and Santato, C. (2024). A study of the doping process in Li4Ti5O12 and TiO2 battery electrode materials studied in the ion-gated transistor configuration. J. Mater. Chem. C Mater. *12*, 2416–2422. https://doi.org/10.1039/D3TC03517D.

40. Wu, Q., Li, W., Cheng, Y., and Jiang, Z. (2005). Homogenous LiCoO2 nanoparticles prepared using surfactant P123 as template and its application to manufacturing ultra-thin-film electrode. Mater. Chem. Phys. *91*, 463–467. https://doi.org/10.1016/j.matchemphys.2004.12.011.

41. Staffolani, A., Darjazi, H., Carbonari, G., Maroni, F., Gabrielli, S., and Nobili, F. (2021). Fe3O4/Graphene Composite Anode Material for Fast-Charging Li-Ion Batteries. Molecules *26*, 4316. https://doi.org/10.3390/molecules26144316.

42. Sayago, J., Soavi, F., Sivalingam, Y., Cicoira, F., and Santato, C. (2014). Low voltage electrolyte-gated organic transistors making use of high surface area activated carbon gate electrodes. J. Mater. Chem. C *2*, 5690–5694. https://doi.org/10.1039/C4TC00864B.

43. Niemöller, A., Jakes, P., Eichel, R.-A., and Granwehr, J. (2019). In operando EPR investigation of redox mechanisms in LiCoO2. Chem. Phys. Lett. *716*, 231–236. https://doi.org/10.1016/j.cplett.2018.12.022.

44. Conway, B.E. (1999). Electrochemical Supercapacitors Scientific Fundamentals and Technological Applications (Springer). https://doi.org/10.1007/978-1-4757-3058-6.

45. Mastragostino, M., and Soavi, F. (2021). Pseudocapacitive and Ion-Insertion Materials: A Bridge between Energy Storage, Electronics and Neuromorphic Computing. Chemelectrochem *8*, 2630–2633. https://doi.org/10.1002/celc.202100457.

46. Jiang, Y., and Liu, J. (2019). Definitions of Pseudocapacitive Materials: A Brief Review. Energy. Environ. Materials *2*, 30–37. https://doi.org/10.1002/eem2.12028.

47. Okubo, M., Hosono, E., Kim, J., Enomoto, M., Kojima, N., Kudo, T., Zhou, H., and Honma, I. (2007). Nanosize Effect on High-Rate Li-Ion Intercalation in LiCoO2 Electrode. J. Am. Chem. Soc. *129*, 7444–7452. https://doi.org/10.1021/ja0681927.

48. Lindberg, S., Jeschke, S., Jankowski, P., Abdelhamid, M., Brousse, T., Le Bideau, J., Johansson, P., and Matic, A. (2020). Charge storage mechanism of α-MnO2 in protic and aprotic ionic liquid electrolytes. J. Power Sources *460*, 228111. https://doi.org/10.1016/j.jpowsour.2020.228111.

STAR★METHODS

KEY RESOURCES TABLE

REAGENT or RESOURCE	SOURCE	IDENTIFIER
Chemicals, peptides, and recombinant proteins		
$LiCoO_2$	Sigma Aldrich	CAS ID: 12190-79-3
NMP	Sigma Aldrich	CAS ID: 872-50-4
PVDF	Arkema	CAS ID: 872-50-4
Carbon paper	Spectracarb	CAS ID: 7782-42-5
Super P	Imerys	CAS ID: 1333-86-4
Durapore PVDF membrane	Sigma-Aldrich	CAS ID: 24937-79-9
Activated carbon	Sigma-Aldrich	CAS ID: 7440-44-0
LiTFSI	Sigma-Aldrich	CAS ID: 90076-65-6
[EMIM][TFSI]	Iolitec	CAS ID: 174899-82-2
$[PYR_{14}][TFSI]$	Iolitec	CAS ID: 223437-11-4

METHOD DETAILS

LCO composite ink

The LCO composite ink was prepared using LCO powder, conductive carbon (Super P conductive carbon black, Imerys) as conductive additive and polyvinylidene fluoride (PVDF) in *N*-methyl-2-pyrrolidone (NMP) solution. The final composition of the ink including LCO, conductive carbon, and PVDF in NMP was 8:1:1 in weight ratio.

Ion-gating media

The ionic liquid 1-ethyl-3-methylimidazolium bis(trifluoromethylsulfonyl)imide, ([EMIM][TFSI], and 1-Butyl-1-methylpyrrolidinium bis (trifluoromethylsulfonyl)imide ($[PYR_{14}][TFSI]$), Iolitec, 99% purity) were purified overnight at 60°C under vacuum conditions. In order to gate in the presence of Li^+, 0.1 and 1 M of LiTFSI (bis(trifluoromethane)-sulfonimide lithium salt (LiTFSI, Sigma-Aldrich, 99.95% purity)) was dissolved in purified [EMIM][TFSI] and $[PYR_{14}][TFSI]$ respectively.

Electrodes fabrications

Source and drain

Drain and source Au/Ti electrodes were patterned on SiO_2/Si wafers by photolithography and deposited by e-beam evaporation. The thickness of the electrodes was 55 nm (5 nm of Ti as adhesion layer, 50 nm of Au). Channel length (interelectrode distance) and width were 10 μm and 4 mm, respectively (Figure S3).

Gates

Carbon paper (6 mm x 3 mm x 170 μm, Spectracarb 2050 A) was coated with an ink containing activated carbon and PVDF in NMP. After coating, the electrodes were thermally treated overnight in a vacuum oven, at 60°C. The activated carbon reference electrode potential is 3 V vs. Li^+/Li.[49]

LCO films deposition

The ink of LCO composite (5 μL) was drop-casted between drain and source Au/Ti electrodes patterned on SiO_2/Si substrate and dried overnight in a vacuum oven, at 80°C. The average thickness of LCO composite films measured by the profilometer was 18 ± 1 μm.

Device assembly

IGT with LCO composite channel was assembled in a N_2 glove box ($[O_2]$ and $[H_2O]$ < 5 ppm). A Durapore PVDF membrane (9 mm × 4 mm, 125 μm-thick) soaked with [EMIM][TFSI] or $[PYR_{14}][TFSI]$ with/without Li^+ was placed on the transistor channel. Finally, the reference/counter or gate electrode was placed on the top of the separator membrane (Figure S3).

Electrochemical response and IGT characterization

Cyclic voltammetry was performed using VersaSTAT4 potentiostat. The transistor characteristics were measured in a home-micromanipulated electrical probe station using an Agilent B1500A semiconductor parameter analyzer.

Five transistors were characterized with [EMIM][TFSI] and 0.1M [LiTFSI] in [EMIM][TFSI] as gating media and three for [PYR_{14}][TFSI] without/with Li^+. A total of 6 cycles were run for cyclic voltammetry (3 cycles) and transistor characterizations (3 cycles). Cycle 2 is reported in all figures.

Material characterizations

The profilometer (DektakXT, model: Bruker) has been used to measure the thickness of the LCO composite films. The morphological structure of the film was studied by scanning electron microscopy (SEM, model: JEOL JMS-7600F), at an accelerating potential of 15 kV. The crystal structure of LCO composite was analyzed by X-ray diffraction (XRD, model: Bruker D8), using a Cu-Kα source (wavelength $\lambda = 1.54$ Å).